

Effect of in-flight annealing and deposition method on gas-sensitive SnO_x films made from size-selected nanoparticles

M.K. Kennedy^a, F.E. Kruis^{a,*}, H. Fissan^a, H. Nienhaus^b, A. Lorke^b, T.H. Metzger^c

^a University Duisburg-Essen, Faculty of Engineering Sciences, Bismarckstraße 81, D47057 Duisburg, Germany

^b University Duisburg-Essen, Solid State Physics, Institute of Physics, Lotharstr.1, D-47048 Duisburg, Germany

^c European Synchrotron Radiation Facility, BP 220, 38043 Grenoble Cedex, France

Received 12 July 2004; received in revised form 20 January 2005; accepted 20 January 2005

Available online 10 May 2005

Abstract

A method which includes synthesis of SnO nanoparticles, size-selection, in-flight oxidation, film formation and post-deposition annealing in oxygen has been investigated. High-temperature in-flight annealing of SnO nanoparticles in the presence of oxygen allowed to assess the effect of this short-time annealing in comparison to post-deposition annealing at lower temperature. This high-temperature annealing was performed in-flight and allowed to keep the crystal size constant, whereas post-deposition high-temperature annealing would have led to crystal growth. Its effect on crystal structure, surface stoichiometry and normalized conductance in ethanol-containing air was investigated. Furthermore, the influence of different particle deposition methods on the crystal phase is shown. Finally, the results indicated that the form of the response transients was markedly different for different gases.

© 2005 Elsevier B.V. All rights reserved.

Keywords: Tin oxide; Nanoparticle; Gas-sensing; In-flight oxidation

1. Introduction

The gas-sensing mechanism of metal-oxide materials depends on chemical and electronic properties and on the three-dimensional ordering of both the bulk and the surface material, and is mainly influenced by the surface region of the grains. Göpel et al. emphasized that the development and improvement of a chemical sensor requires a balance between empirical knowledge and systematic research as long as the basic processes involved are unknown [1]. SnO₂ gas sensors are one of the examples of functional materials where the use of nanoparticles was shown to lead to improved sensor properties [2,3]. Nanoparticles form porous films, thus maximizing the surface area which is accessible to the gas. Accordingly, studying the structure as well as the chemical composition, is of great importance to better understand the gas-sensing mechanism [4].

Generally, non-stoichiometric tin oxide (SnO_{2-x}) is used as sensing material. Oxygen vacancies are necessary for the adsorption and desorption of ionized oxygen species, which depend on the temperature. Typical chemisorption species on the surface of tin oxide are O₂⁻ and O⁻ [5]. In spite of many studies concerning the oxidation of SnO_x thin films prepared from Sn or SnO₂ [6], only a little amount of work on the oxidation process of SnO nanoparticles can be found in the literature. Even less is known on the influence on the gas sensing behavior. The main problem here is that oxidation is promoted at higher temperatures, i.e. deposited samples are treated at elevated temperatures, leading to changes in crystallite size due to solid state sintering.

It is known that annealing treatments influence the normalized conductance of SnO₂ thin film gas sensors [7]. However, this can be due to changes in crystallite size as well as in the crystal phase. The best-known crystallographic structures of SnO₂ are orthorhombic and tetragonal [8]. The tetragonal structure is, generally, thermodynamically more stable. Using EPR (electron paramagnetic resonance) it was found

* Corresponding author. Fax: +49 203 379 3268.

E-mail address: e.kruis@uni-duisburg.de (F.E. Kruis).

that a strong adsorption of O_2^- and O^- on SnO_2 films having a mixture of the orthorhombic and tetragonal phase occurred, whereas O^- appear predominantly on a fully tetragonal SnO_2 phase. If hydrogen is to be detected the O^- species plays a major role. Therefore, the occurrence of orthorhombic crystallographic structure lowers the sensitivity to hydrogen detecting [9]. Additionally, orthorhombic crystallographic SnO_2 structure is detected if a mechanical milling process is carried out but an effect on the gas-sensing properties was not investigated [10]. In most synthesis experiments one has to change the synthesis conditions drastically in order to change the crystal phase, so that the influence of the crystal phase on the sensing behavior becomes difficult to be understood.

In our previous work the synthesis and characterization of tailored thin films based on size-selected SnO_x nanoparticles for gas-sensing application was studied [3]. It has been demonstrated that the gas-sensing properties depend on the particle size in the range of 10–35 nm. The effect was especially evident for particles sizes below 20 nm. However, not only the particle size effects on the sensing behavior but also the chemical composition is important because the amount of oxygen vacancies can influence the number of chemisorbed oxygen species and, thus, the conductivity change due to this process.

To vary the normalized conductance of a metal-oxide gas sensor, different methods exist, such as doping [18,19], producing a second metal-oxide phase in the sensing layer [20] and, as presented in this investigation, varying the particle size. In this work, a simpler way to increase the normalized conductance will be described. This investigation will show how the process parameters of the synthesis set-up affect the nanoparticle properties and the gas-sensing properties of the nanoparticle films generated and, consequently, will provide information to enable the material dependent properties of defined SnO_x gas sensors produced in the gas phase to be better understood.

2. Experimental procedure

The fabrication of well-defined SnO_x nanoparticle films was described earlier in more detail [11]. The experimental setup consisted of an evaporation–condensation aerosol reactor in which SnO powder was sublimated in flowing carrier gas. The aerosol formed was then size-fractionated by means of a differential mobility analyzer (DMA). The resulting monodisperse aerosol was then passed through another tube furnace in which the aggregates were sintered in-flight for ~ 1 s at $650^\circ C$ into quasi-spherical monocrystalline nanoparticles. Furthermore, in this furnace oxygen could be added for oxidation into SnO_2 . The procedure allowed to fabricate almost equal sized nanoparticles with a very good crystallinity, in which the size could be selected independently from the synthesis conditions. The particle diameter

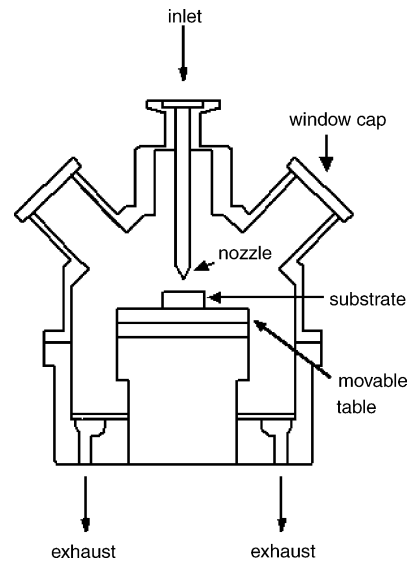


Fig. 1. Schematic of the advanced electrostatic precipitator for a more localized deposition of nanoparticles by means of low pressure impaction. The window caps and movable table are needed to adjust the position of the substrate accurately.

after the sintering step as determined with the DMA (mobility equivalent diameter) was denoted as D_{ms} .

The thus formed tin oxide aerosol is then deposited in form of a thin film. Two deposition methods were investigated in this study: an electrostatic precipitator (ESP) [16]; and a low pressure impactor (LPI). The main purpose of the LPI is to obtain a more localized deposition area, whereas the ESP typically produces a film area of $0.5\text{--}1\text{ cm}^2$ is this for the LPI below 1 mm^2 . This is effective for fast deposition on microhotplates with a small sensor area [15]. The LPI is a modification of the ESP housing by adding a nozzle with an inner diameter of 0.5 mm which is positioned 2 mm above the substrate and a critical nozzle placed in the inlet tube (Fig. 1). The critical nozzle allows to create a low pressure (2.7 mbar) in the LPI chamber by means of a rotary pump.

The microhotplates consisted of a 1 mm^2 structure consisting of 160 interdigitated fingers with a width of $2\text{ }\mu\text{m}$ and identical separations was fabricated on a chip of $3\text{ mm} \times 3\text{ mm}$ size. The electrodes were buried in the phosphor-doped silicate glass having a resistance value much higher than the nanoparticle sample and a viscous behavior required for processing. The resistance of the structure without the deposited film is more than $1000\text{ G}\Omega$ at room temperature and $5\text{ G}\Omega$ at $300^\circ C$ and thus is suitable for high-resistance ($\sim 10\text{ M}\Omega$) nanoparticle layers. The electrode consisted of platinum and was buried in order to eliminate the influence of electrode walls on the particle deposition.

The inertial focusing of the nanoparticle aerosol resulted in a deposition spot with a diameter of $500\text{ }\mu\text{m}$ when using an 0.5 mm nozzle so that a deposition area of $2 \times 10^{-7}\text{ m}^2$ can be assumed as a mean value. Consequently, layers with a thickness of more than 100 nm using size-selected nanoparticles in the range of 10–35 nm could be formed rapidly. Two

window caps, together with a movable table, are necessary to control the position of the substrate below the nozzle. If a SnO₂ nanoparticle film with a particle diameter of 20 nm and a layer thickness of 1 μm is to be generated, this would need approximately 4 h for a particle number concentration of 10¹⁰ particles/m³. The particle concentration cannot be too high, because Brownian coagulation will then lead to collision in the sintering and oxidation furnace which leads to loss of the monodispersity and spherical shape of the particles. The size-selection step automatically leads to a reduction of the number concentration so that no collisions take place in the high-temperature zone.

To interpret gas-sensing properties in connection to material properties the morphology and the chemical composition of the sensing layer was investigated. The SnO_x nanoparticle films were investigated by means of X-ray radiation from a synchrotron source in order to analyze the crystallographic structure of the films. The width of the X-ray reflection peaks was determined by the number of the reflecting lattice planes and increases as the crystallite size decreases. The mean crystallite size d was calculated by the Scherrer equation using the Bragg peak broadening effect:

$$d = \frac{K\lambda}{\beta \cos \Theta} \quad (1)$$

where d is the mean crystallite size; K is a grain shape-dependent constant (here assumed to be 1); λ is the wavelength of the incident beam; Θ is the Bragg reflection peak; and β is the full width of half maximum. The measured Bragg peak width value consists of the full width of half maximum β and a value b given by the resolution of the diffractometer. b is determined by a diffraction phenomenon at the aperture:

$$\beta = \sqrt{(b^2 + \beta_{\text{real}}^2)} \quad (2)$$

It has been demonstrated that the strain and shape of quantum dots can be separated by means of grazing incidence X-ray scattering. In this case, the intensity along the angular direction at different positions was analyzed [12]. If the diffraction peak broadening has a Lorentz profile, this is caused mainly by crystallite size effects. A Gauß profile would indicate microstrains inside the crystal lattice [13]. X-rays from synchrotron sources have the advantage that the incoming beam has such a high intensity that the measurements can be done on small amounts of nanoparticle layers.

In this investigation, θ – 2θ scans of SnO_x nanoparticle films on silicon substrates are measured under a grazing incidence angle of 1°. X-ray diffraction from synchrotron sources (incoming beam energy 8 keV) at the European Synchrotron Radiation Facility (ESRF) in Grenoble/Switzerland was carried out with different mobility-equivalent diameters in the range of $D_{\text{mi}} = 10$ – 25 nm after in-flight sintering. As-deposited nanoparticles as well as annealed nanoparticle layers were investigated. The mean crystallite size of size-selected, in-flight sintered SnO was calculated from the line-

Table 1

Comparison of the mean particle size after sintering measured with DMNPS and TEM and the mean crystallite size calculated with the XRD data for different initial mobility particle diameters D_{mi}

D_{mi} (nm)	DMNPS (nm)	TEM (nm)	XRD (nm)
15	10.5	9.6	7.3
25	14.5	14.0	14.9
32	18.3	18.8	17.5
45	24.5	24.2	23.3

broadening of all Bragg peaks, and was compared with those obtained from TEM measurements on samples deposited on a TEM grid and from online measurements of the mobility-equivalent diameter by means of DMA. Table 1 shows the crystallite size compared to particle size values measured by means of DMA and by TEM analysis. The values agree quite good, so that indeed the particles are monocrystalline. The larger difference detected in measuring the 10 nm sample might have occurred due to the fact that only one Bragg peak could be used to calculate the crystallite size.

In order to investigate the gas-sensing properties with the knowledge of the material properties, especially the surface stoichiometry is essential. Therefore, Auger electron spectroscopy (AES) measurements have been performed on the SnO_x nanoparticle layers [14]. The base pressure in the analysis chamber was below 10^{−9} hPa. AES spectra were recorded in the first derivative mode and the energy of the primary electron beam was adjusted to 3 keV. The oxygen stoichiometry was estimated from the ratio of the Auger peak-to-peak heights of the O(KLL) line at a kinetic energy of 510 eV and the low-energy feature of the Sn(MNN) doublet at 421 eV. The AES spectrum of sintered SnO₂ powder was used as a calibration reference for determining the oxygen content in the SnO_x nanoparticles.

For measurements of the sensitivity and dynamic behavior of a nanoparticle gas sensor, a picoamperemeter (model 487, Keithley Instr./Germany) with an internal voltage source was used. The instruments were connected via an IEEE-488 bus to the computer. The set-up can be used to measure gas-sensing characteristics in well-defined temperature cycles and gas concentration levels [15]. The sensing gas must be introduced into a defined reaction volume. This volume is assured by a closed measurement chamber with feedthroughs for preparing the electrical connections for resistance measurement and for heating and temperature control. During the measurement a constant gas flow of 150 ml/min was maintained in the chamber. It is essential to purge the tubes and the measurement chamber volume before its commencement to ensure stable experimental conditions; adequate purging of the system is achieved by allowing nitrogen or synthetic air without any humidity to flow for a minimum period of 30 min. Long-time (several days) measurements are possible in predetermined gas ambients and temperature cycles without the need of an operator. A virtual instrument allowed an easy control of the different experimental conditions used in gas sensor characterization [15].

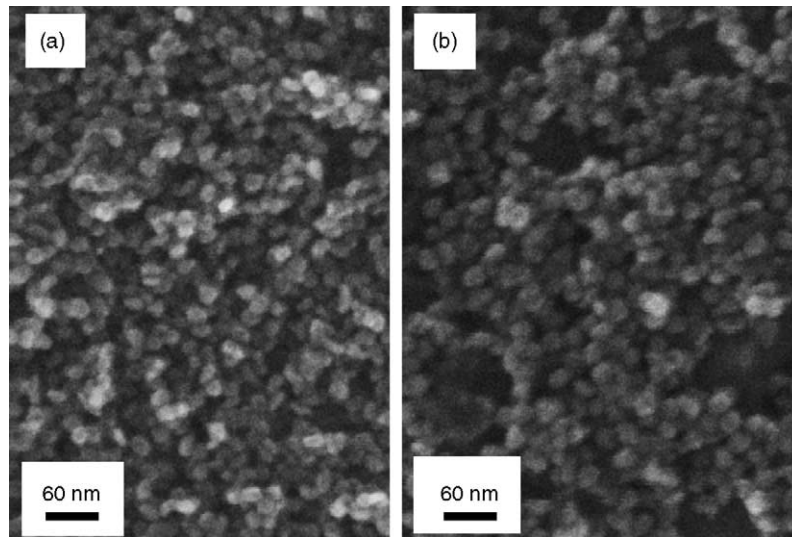


Fig. 2. SEM micrograph of a nanoparticle ($D_{ms} = 20$ nm) film made by LPI composed of (a) size-fractionated as-deposited SnO nanoparticles and (b) after annealing at 300 °C for 1000 h in synthetic air containing ethanol.

3. Results and discussion

3.1. Effect of annealing of nanoparticle film on particle morphology

For efficient gas sensing the particle layer should have a porous structure to enable rapid chemisorption. Therefore, scanning electron microscopy (SEM) was used mainly to show the surface morphology of as-deposited and annealed nanoparticle layers and also provided information about the design of the microhotplates used for gas-sensing measurements. Fig. 2 shows SEM (LEO 1530, LEO Elektronenmikroskopie GmbH, Germany) micrographs of a nanoparticle film composed of size-fractionated ($D_{ms} = 20$ nm) SnO nanoparticles as-deposited (Fig. 2(a)) and after annealing at 300 °C for 1000 h in ethanol-containing synthetic air (Fig. 2(b)). An equal grain size, a uniform film formation, a compact film structure and a good connectivity between the particles can be recognized. No difference between the nanoparticle film which was annealed and the unannealed nanoparticle film can be seen. This was supported by XRD measurements, which did not detect a change in crystallite size after annealing. Due to insufficient resolution the sintering necks connecting individual particles which most likely will be present after the annealing cannot be seen in the SEM. These necks enable current transport through the film. Furthermore, the uniform grain size ensures a similar neck formation rate for all particles without changing the grain size.

3.2. The influence of in-flight oxidation on the crystallographic structure

The influence of the various process parameters on the crystallographic structure of nanoparticle layers was investigated. One of the most important process parameters is

the oxidation step, as the aerosol which is produced by the evaporation–condensation is SnO. The θ – 2θ plots for size-fractionated nanoparticles with different mobility-equivalent diameters in the range of $D_{ms} = 10$ –25 nm after in-flight sintering at 650 °C without the addition of oxygen are shown in Fig. 3. For particle sizes over 15 nm, the predominant peaks can be observed at $2\theta = 21.11^\circ$ ($d = 4.88$ Å), $2\theta = 34.4^\circ$ ($d = 3.002$ Å), $2\theta = 38.88^\circ$ ($d = 2.689$ Å) and $2\theta = 43.13^\circ$ ($d = 2.435$ Å) correspond to the (001), (101), (110) and (002) planes of the tetragonal SnO (romarchite) phase. The (101) and the (110) planes could also be detected for 10 nm particles which showed a strong peak broadening. No Bragg peaks corresponding to known SnO₂ phases were found.

Thus, an oxidation step is necessary to obtain a SnO₂ phase. If 10 vol.% oxygen was added to the nitrogen carrier gas during the in-flight sintering furnace at 650 °C, both the tetragonal as well as the orthorhombic SnO₂ phase was detected (Fig. 4). “O” denotes the position

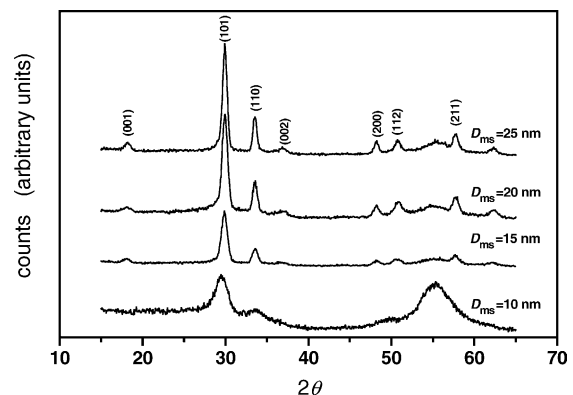


Fig. 3. θ – 2θ scans of nanoparticle films composed of size-fractionated SnO nanoparticles of different diameters (D_{ms}) deposited with LPI without the addition of oxygen in the second furnace. The lattice planes of tetragonal SnO are indicated.

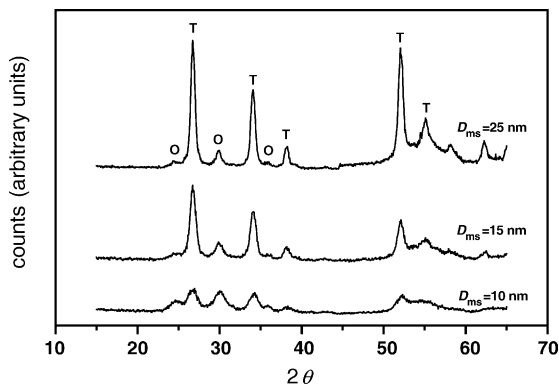


Fig. 4. θ – 2θ scans of nanoparticle films composed of size-fractionated SnO_x nanoparticles of different diameters (D_{ms}). The particles were oxidized in-flight in 10 vol.% oxygen in the sintering furnace at 650°C . “O” denotes the position of the Bragg peaks for orthorhombic SnO_2 and “T” the position of the Bragg peaks for tetragonal SnO_2 planes.

of the Bragg peaks for orthorhombic SnO_2 and “T” the position of the Bragg peaks for tetragonal SnO_2 . The Bragg peaks at $2\theta = 24.4^\circ$ ($d = 3.64 \text{ \AA}$), $2\theta = 29.8^\circ$ ($d = 2.984 \text{ \AA}$) and $2\theta = 35.7^\circ$ ($d = 2.609 \text{ \AA}$) clearly point to the (1 1 0), (1 1 1) and (0 0 2) planes of orthorhombic SnO_2 ; $2\theta = 31.04^\circ$ ($d = 3.34 \text{ \AA}$), $2\theta = 34.4^\circ$, $2\theta = 39.63^\circ$ ($d = 2.64 \text{ \AA}$) and $2\theta = 44.27^\circ$ ($d = 2.375 \text{ \AA}$) clearly point to the (1 1 0), (1 0 1) and (2 0 0) planes of the tetragonal SnO_2 phase. The tetragonal phase is more dominant than the orthorhombic one. An increase in the oxygen concentration during in-flight oxidation did not change the crystallographic structure, nor did annealing of the films in synthetic air at 400°C for 1 h.

3.3. The influence of film annealing in oxygen and the deposition method on the crystallographic structure

One of the key questions with respect to the oxidation is whether the in-flight high-temperature oxidation is necessary or not. Gas-sensing films are usually ‘activated’ by exposing it to oxygen at elevated temperatures. In Fig. 5 θ – 2θ

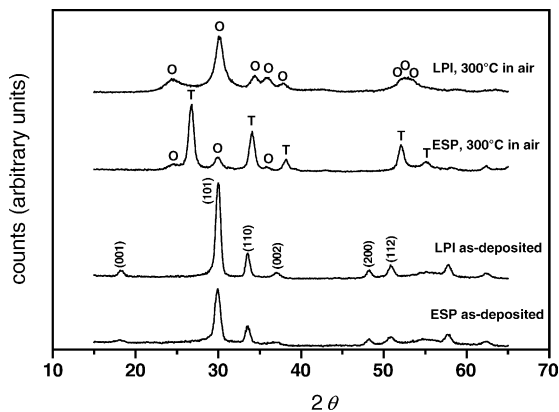


Fig. 5. θ – 2θ scans of nanoparticle films composed of size-fractionated SnO nanoparticles with $D_{ms} = 20 \text{ nm}$ using an ESP and LPI. Both samples were post-annealed at 300°C in synthetic air for 2 h.

plots of size-selected SnO nanoparticles with $D_{ms} = 20 \text{ nm}$ which were post-annealed in synthetic air for 2 h at 300°C are shown. For a comparison, the results for as-deposited films consisting of SnO nanoparticles are shown. Furthermore, the results are shown for both the ESP as well as LPI deposition technique.

From Fig. 5, it can be seen that the deposition technique does not have an influence on the crystal phase in case of the as-deposited SnO nanoparticles. The post-annealing of the SnO nanoparticle film leads to SnO_2 crystal phases. But, unexpectedly, the deposition technique seems to have an influence on which SnO_2 phase is formed. If the LPI method is used, the nanoparticle layer consists of an orthorhombic SnO_2 phase, whereas a mixture of a tetragonal and orthorhombic SnO_2 appears if the ESP method is used for the deposition of the nanoparticles.

This difference can only be due to the different impact velocities of the nanoparticles on both the substrate and the already deposited nanoparticles. The impact velocity of the nanoparticles was on the order of 1 m/s for the ESP method, whereas a much higher velocity was reached when the particles were accelerated through a critical orifice and expanded in a low-pressure region, so that they could reach sonic velocities of a few hundreds m/s. It was not possible to directly relate this impact velocity to a different crystal structure because of a higher pressure inside the nanoparticle during impact, as both deposition techniques showed SnO after deposition. These phenomena can be explained by a modified oxidation process when using the LPI deposition method caused by a different morphology of the deposit; it results in a metastable SnO_2 phase. Because of the much higher impact velocity of nanoparticles during the LPI process, it is assumed that an LPI method will create more dense particle layers than when using an ESP. A possible explanation is that the particles which are not in-flight oxidized are deposited in the form of a meta-stable intermediate orthorhombic phase, which is easily transformed at 300°C to the more stable tetragonal phase under the influence of oxygen. However, the LPI deposit is probably much more dense, and the oxygen diffusion through the film is much slower than in case of the presumably open and porous films in case of the ESP deposition, so that this transformation was not completed due to a much decreased oxygen transport through the film.

3.4. Effect of in-flight and post-deposition oxidation on the surface stoichiometry

For the analysis of gas-sensing properties of SnO_2 nanoparticle films not only the crystallographic structure is of importance but also the stoichiometry, especially at the surface. Table 2 shows the stoichiometry changes induced by in-flight oxidation at 650°C (for 1 s) and post-deposition annealing at 300°C (for 2 h) in synthetic air [14]. The most interesting result is that when the nanoparticles are in-flight oxidized at high temperature, the stoichiometry after post-deposition low-temperature annealing was always close to

Table 2

Oxygen content x in SnO_x nanoparticle films as a function of oxygen concentration during in-flight high-temperature oxidation and as a function of post-deposition low-temperature annealing in synthetic air [14]

Oxygen supply (vol.%)	Stoichiometry (SnO_x)		
	As-deposited	Annealed once at 300 °C in synthetic air	Annealed twice at 300 °C in synthetic air
0	1.2	1.9	2
10	1.5	1.8	1.8
20	1.75	1.8	1.76
35	1.85	1.8	1.8

$\text{SnO}_{1.8}$. When they were not in-flight oxidized, the stoichiometry was $\text{SnO}_{1.9}$ after one annealing step and becomes $\text{SnO}_{2.0}$ after prolonged annealing. Thus, for a given heat treatment, the final stoichiometry of the particles is dependent on its previous history during synthesis. The high-temperature oxidation, even only for approximately 1 s, seems to stabilize the nanoparticles such that even a prolonged oxidation at 300 °C has little influence. It is important to note that a stoichiometry below 2.0 is expected to be advantageous for gas sensing, as oxygen vacancies are needed for the charge transport. Furthermore, the operation temperature is often around 300 °C, so that a structural stability during operation in oxygen-containing atmosphere at this temperature is advantageous in terms of sensor stability. From oxidation studies of thin SnO films, it is known that the transformation into SnO_2 occurs during heating at 500–600 °C for 1 h, either directly or by passing through an intermediate phase of Sn_3O_4 [17]. In this investigation, in-flight oxidation occurred within a much shorter time scale (0.5 s).

3.5. Influence of in-flight oxidation on gas-sensing behavior SnO_2 nanoparticle layers

It has been demonstrated how the variation of the process parameter during the synthesis and deposition can influence the properties of the nanoparticle films, most importantly the crystal phase and surface stoichiometry. Fig. 6 shows the normalized conductance (often referred to in the literature as “sensitivity”) in 1000 ppm ethanol as a function of operating temperature for samples having $D_{\text{ms}} = 10$ nm (NF10), and

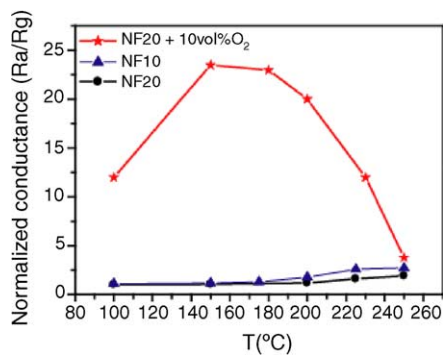


Fig. 6. Normalized conductance of NF10, NF20 and in-flight oxidized NF20 as a function of the operating temperature in 1000 ppm ethanol. Film thickness is 1.5 μm , the deposition technique is LPI.

$D_{\text{ms}} = 20$ nm (NF20) which were not in-flight oxidized. It also shows results for $D_{\text{ms}} = 20$ nm (NF20) which was in-flight oxidized with 10 vol.% oxygen at 650 °C for 0.5 s. All samples were annealed after deposition in synthetic air at 300 °C. Compared to the samples which were not in-flight oxidized in the gas phase, the maximum normalized conductance of an in-flight oxidized SnO_2 nanoparticle sample is nearly one order of magnitude higher. The maximum normalized conductance shifts towards a lower operating temperature.

We can now relate this higher normalized conductance to the results of the crystallographic investigations and the AES measurements. Based on the AES results, the in-flight oxidation leads to more sub-stoichiometric tin oxide, around $\text{SnO}_{1.8}$. A lower stoichiometry results in a higher concentration of ionized donor atoms N_d and, therefore, in a larger value for thickness of the space charge region L_D :

$$L_D = \sqrt{\frac{2\epsilon_r\epsilon_0N_d}{eN_s^2V_s}} \quad (3)$$

so that a larger portion of these small particles is depleted. This will lead to higher normalized conductance values.

Furthermore, the absence of in-flight oxidation and deposition by LPI led to the orthorhombic SnO_2 crystal phase, whereas high-temperature in-flight oxidation leads to a mainly tetragonal crystal structure. From this, we can conclude that the thermodynamically more stable tetragonal phase [13] and surface sub-stoichiometry (here $\text{SnO}_{1.8}$) is apparently responsible for the higher normalized conductance towards ethanol below 300 °C.

3.6. Response transients for different gases

There is a continually increasing interest in the production of a selective gas sensor. Many different methods have been followed: for instance, film thickness has a great influence on normalized conductance. Sakai et al. assumed that the molecular weight of the gas is responsible for different normalized conductance values [21]. They explained this by using the Knudsen diffusion equation assuming that the gas reaction follows first-order kinetics with respect to the gas concentration and, therefore, a calculation of the concentration profile for different gases in the pores of the sensing material can be made. We studied the response transients for different gas types as we expect that the form of the electrical resistance versus time for both the reaction and the recovery processes

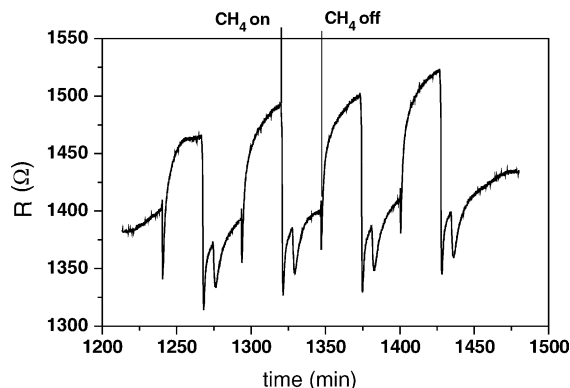


Fig. 7. Response transients on switching the methane flow on and off (D_{ms} : 20 nm, $T = 270^\circ\text{C}$; concentration 1000 ppm).

will be a function of the gas type. Due to the fact that the chemical reaction of the gas with the sensing surface can produce intermediate products with different reaction rates, it will influence the oxygen adsorption and desorption reaction. 1000 ppm methane is introduced into the measurement chamber and resistance measurements are carried out with the NF20 sample at 270°C (Fig. 7). The reaction and recovery processes are repeated four times. It can be seen that introduction of methane is followed by two minima. The form of the response transient methane under these conditions is reproduced very well.

If hydrogen is detected by the same sample under the same conditions (gas concentration; temperature), the slope of the response transient is different compared to that of methane or ethanol. The response transients for hydrogen are presented in Fig. 8. Introduction of H_2 leads to a rapid decrease in the resistance and then a more gradual increase towards a steady state. No further peaks in the response transient were detected. The recovery process in Fig. 7 is also different compared to that using hydrogen, as shown in Fig. 8. Introduction of synthetic air for sensor recovery leads to a stable value via a maximum in the response transient. Here also, the process can be repeated, leading to identical forms of the response transients. Further investigations are necessary to explain these

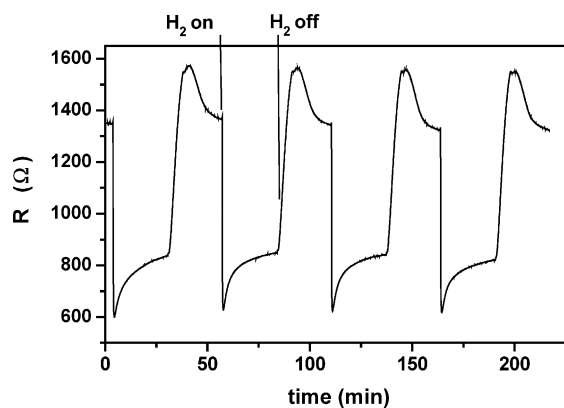


Fig. 8. Response transients on switching the H_2 flow on and off (D_{ms} : 20 nm, $T = 270^\circ\text{C}$; concentration 1000 ppm).

results in a detailed form. Clearly, the response transients will depend on the transport properties of the different gas molecules in the film, the activation energy for the chemical reactions and the electrical properties of the sensing layer itself.

4. Conclusions

High-temperature annealing of SnO nanoparticles in the presence of oxygen allowed to assess the effect of this short-time annealing in comparison to post-deposition annealing at lower temperature. This high-temperature annealing was performed in-flight and allowed to keep the crystal size constant, whereas post-deposition high-temperature annealing would have led to crystal growth. The high-temperature annealing in oxygen led to a sub-stoichiometric particle surface even after post-deposition annealing ($\text{SnO}_{1.8}$) whereas values closer to stoichiometric SnO_2 were found when leaving out the high-temperature step. The sensor films composed of in-flight treated tin oxide showed higher normalized conductance values. Interestingly, different particle deposition methods led to different crystal structures of SnO_2 when the nanoparticle films are post-treated, even when the as-deposited films produced without the in-flight oxidation step had the same SnO crystal structure. This might be explained by a different film density due to the impact velocities being very different, so that oxygen transport into the film is influenced. Finally, the results indicated that the form of the response transients was markedly different for different gases.

Acknowledgements

This work was supported by the German National Science Foundation (DFG) in the framework of the Collaborative Research Center on ‘Nanoparticles from the gas phase: formation, structure and properties’ (SFB 445).

References

- [1] W. Göpel, K.D. Schierbaum, SnO_2 sensors: current status and future prospects, *Sens. Actuators B* 26 (1995) 1–12.
- [2] N.S. Baik, G. Sakai, K. Shimano, N. Miura, N. Yamazoe, Hydrothermal treatment of tin oxide sol solution for preparation of thin-film sensor with enhanced thermal stability and gas sensitivity, *Sens. Actuators B* 65 (2000) 97–100.
- [3] M.K. Kennedy, F.E. Kruijs, H. Fissan, B.R. Mehta, S. Stappert, G. Dumpich, Tailored nanoparticle films from monosized tin oxide nanocrystals: particle synthesis, film formation, and size-dependent gas-sensing properties, *J. Appl. Phys.* 93 (2003) 551–560.
- [4] G. Martinelli, M.C. Carotta, E. Traversa, G. Ghiotti, Thick-film gas sensors based on nano-sized semiconducting oxide powders, *MRS Bull.* 24 (1999) 30–36.
- [5] S.C. Chang, Oxygen chemisorption on tin oxide: correlation between electrical conductivity and EPR measurements, *J. Vac. Sci. Technol.* 17 (1980) 366–369.

- [6] K.S. Yoo, N.M. Cho, H.S. Song, H.J. Jung, Surface morphology and gas-sensing characteristics of SnO_{2-x} thin films oxidized from Sn films, *Sens. Actuators B* 25 (1995) 474–477.
- [7] Q. Pan, J. Xu, X. Dong, J. Zhang, Gas-sensitive properties of nanometer-sized SnO_2 , *Sens. Actuators B* 66 (2000) 237–239.
- [8] K. Suito, N. Kawai, Y. Masuda, High pressure synthesis of orthorhombic SnO_2 , *Mater. Res. Bulletin* 10 (1975) 677–680.
- [9] J.P. Ahn, S.H. Kim, J.K. Park, M.Y. Huh, Effect of orthorhombic phase on hydrogen gas sensing property of thick-film sensors fabricated by nanophase tin dioxide, *Sens. Actuators B* 64 (2003) 125–131.
- [10] Ü. Kersen, The gas-sensing potential of nanocrystalline SnO_2 produced by a mechanochemical milling via centrifugal action, *Appl. Phys. A* 75 (2002) 559–563.
- [11] M.K. Kennedy, F.E. Kruis, H. Fissan, Gas phase synthesis of size selected SnO_2 nanoparticles for gas sensor applications, *Mater. Sci. Forum* 343–346 (2000) 949.
- [12] T.H. Metzger, I. Kegel, R. Paniago, J. Peisl, Grazing incidence X-ray scattering: an ideal tool to study the structure of quantum dots, *J. Phys. D* 32 (1999) A202–A207.
- [13] T.H. de Keijser, J.I. Langford, E.J. Mittemeijer, A.B.P. Vogels, Use of the Voigt function in a single-line method for the analysis of X-ray diffraction line broadening, *J. Appl. Cryst.* 15 (1982) 308–314.
- [14] R. Ramamoorthy, M.K. Kennedy, H. Nienhaus, A. Lorke, F.E. Kruis, H. Fissan, Surface oxidation of monodisperse SnO_x nanoparticles, *Sens. Actuators B* 88 (2003) 281–285.
- [15] M.K. Kennedy, F.E. Kruis, H. Fissan, B.R. Mehta, A fully-automated gas-sensing and electronic parameter measurement setup for miniaturized nanoparticle gas sensors, *Rev. Sci. Instr.* 74 (2003) 4908–4915.
- [16] J. Dixkens, H. Fissan, Development of an electrostatic precipitator for off-line particle analysis, *Aerosol Sci. Technol.* 30 (2003) 438–453.
- [17] J. Geurts, S. Rau, W. Richter, F.J. Schmitte, SnO -films and their oxidation to SnO_2 : Raman scattering, IR-reflectivity and X-ray diffraction study, *Thin Solid Films* 121 (1984) 217–223.
- [18] J.P. Li, Y. Wang, X.G. Gao, Q. Ma, L. Wang, J.H. Han, H_2S sensing properties of the SnO_2 -based thin films, *Sens. Actuators B* 65 (2000) 111–113.
- [19] G. Carbajal-Franco, A. Tiburcio-Silver, J.M. Dominguez, A. Sanchez-Juarez, Thin film tin oxide-based propane gas sensors, *Thin Solid Films* 373 (2000) 141–144.
- [20] M. Radecka, K. Zakrzewska, M. Rekas, SnO_2 - TiO_2 solid solutions for gas sensors, *Sens. Actuators* 47 (1998) 194–204.
- [21] G. Sakai, N.S. Baik, N. Miura, N. Yamazoe, Gas sensing properties of tin oxide thin films fabricated from hydrothermally treated nanoparticles: dependence of CO and H_2 response on film thickness, *Sens. Actuators B* 77 (2001) 116–121.